



Characterization of Sentinel-2A and Landsat-8 top of atmosphere, surface, and nadir BRDF adjusted reflectance and NDVI differences

Hankui K. Zhang^{a,*}, David P. Roy^a, Lin Yan^a, Zhongbin Li^a, Haiyan Huang^a, Eric Vermote^b, Sergii Skakun^{b,c}, Jean-Claude Roger^{b,c}

^a Geospatial Sciences Center of Excellence, South Dakota State University, Brookings, SD 57007, USA

^b Terrestrial Information System Laboratory (Code 619), NASA Goddard Space Flight Center, Greenbelt, MD 20771, USA

^c Department of Geographical Sciences, University of Maryland, College Park, MD 20742, USA

ARTICLE INFO

Keywords:

Sentinel-2 MSI
Landsat-8 OLI
Reflectance
NDVI
Differences

ABSTRACT

The medium spatial resolution satellite data from the polar-orbiting Sentinel-2A Multi Spectral Instrument (MSI) and Landsat-8 Operational Land Imager (OLI) sensors provide 10 m to 30 m multi-spectral global coverage with a better than 5-day revisit. There are a number of differences between the sensor data that need to be considered before the data can be used together reliably. Sentinel-2A and Landsat-8 data for approximately $10^\circ \times 10^\circ$ of southern Africa acquired in two summer (December and January) and in two winter (June and July) months of 2016 were compared. The data were registered and each orbit projected into 30 m fixed non-overlapping tiles defined in the sinusoidal equal area projection. Only corresponding sensor observations of each 30 m tile pixel that were both not cloudy, shadow, saturated, or cirrus contaminated, and that were acquired within one-day of each other, were compared. Both the Sentinel-2A MSI and Landsat-8 OLI data were atmospherically corrected using the Land Surface Reflectance Code (LaSRC) and were also corrected to nadir BRDF adjusted reflectance (NBAR). Top of atmosphere (TOA), surface reflectance, and NBAR, for the spectrally corresponding visible, near infrared (NIR) and shortwave infrared (SWIR) MSI and OLI bands, and derived normalized difference vegetation index (NDVI) (from the narrow NIR band for MSI), were compared and their sensor differences quantified by regression analyses. Atmospheric contamination and bi-directional reflectance differences were evident in the 65 million pairs of contemporaneous MSI and OLI observations considered. The MSI surface reflectance was greater than the OLI surface reflectance for all the bands except the green, red, and the broad MSI NIR bands, and the MSI surface NDVI was greater than the OLI surface NDVI. This pattern was also found in the NBAR sensor comparisons except for the red bands. Simulated MSI and OLI reflectance derived using the sensor spectral response functions and laboratory spectra showed similar results in the red, NIR and SWIR bands as the real data comparisons. Ordinary least squares (OLS) linear regressions of the 65 million pairs of contemporaneous MSI and OLI data for the three processing levels had good fits ($r^2 > 0.87$ for the TOA data comparisons, $r^2 > 0.89$ for the atmospherically corrected data comparisons, $r^2 > 0.90$ for the NBAR data comparisons; p -values < 0.0001). The OLS regression coefficients are provided so that they can be used to help improve the consistency between Sentinel-2A MSI and Landsat-8 OLI data.

1. Introduction

The free-availability of Landsat-8 Operational Land Imager (OLI) and Sentinel-2A Multi Spectral Instrument (MSI) data significantly advances the virtual constellation paradigm for mid-resolution land imaging (Roy et al., 2014a; Wulder et al., 2015). In combination, data from Landsat-8, Sentinel-2A and Sentinel-2B will provide global observations on average once every 2.9 days (Li and Roy, 2017). The Sentinel-2 MSI

(Drusch et al., 2012) and Landsat-8 OLI (Irons et al., 2012) are similar but have different spectral and spatial resolution and, therefore, except for certain supervised classification applications, their data cannot be reliably used together. In addition, depending on the sensitivity of the application, correction for atmospheric effects (Hagolle et al., 2015; Vermote et al., 2016; Müller-Wilm, 2016), for surface reflectance anisotropy (Roy et al., 2016a, 2017), and, for sensor misregistration (Yan et al., 2016; Skakun et al., 2017; Storey et al., 2016), may also be

* Corresponding author.

E-mail addresses: hankui.zhang@sdstate.edu (H.K. Zhang), david.roy@sdstate.edu (D.P. Roy), lin.yan@sdstate.edu (L. Yan), zhongbin.li@sdstate.edu (Z. Li), haiyan.huang@sdstate.edu (H. Huang), eric.f.vermote@nasa.gov (E. Vermote), sergii.skakun@nasa.gov (S. Skakun), jean-claude.roger@nasa.gov (J.-C. Roger).

<https://doi.org/10.1016/j.rse.2018.04.031>

Received 15 October 2017; Received in revised form 12 April 2018; Accepted 16 April 2018

Available online 24 April 2018

0034-4257/ © 2018 The Authors. Published by Elsevier Inc. This is an open access article under the CC BY-NC-ND license

(<http://creativecommons.org/licenses/by-nc-nd/4.0/>).

needed.

This paper characterizes Sentinel-2A MSI and Landsat-8 OLI reflectance and normalized difference vegetation index (NDVI) differences. The spectrally overlapping reflective wavelength MSI and OLI bands are compared and statistical functions to transform between them, and the sensor NDVI, are presented. This is undertaken for top of atmosphere (TOA) reflectance and atmospherically corrected surface reflectance. In addition, the surface reflectance data are adjusted to a nadir view and local solar observation geometry to provide nadir bi-directional reflectance distribution function (BRDF) adjusted surface reflectance values that are also compared between sensors. In order to capture a wide range of surface and atmospheric conditions two winter and two summer months of data over 1200×1200 km of southern Africa are examined. More than 65 million spatially corresponding sensor observations extracted from Landsat-8 OLI Collection 1 images and Sentinel-2A L1C tile acquisitions sensed no more than one day apart are examined. As sensor spectral response differences mean that the observed radiance is usually different among sensors (Steven et al., 2003) simulated MSI and OLI reflectance derived using the sensor spectral response functions and laboratory spectra are also compared. Previous researchers have reported comparisons between Sentinel-2A MSI and Landsat-8 OLI data but did not consider BRDF correction (Mandanici and Bitelli, 2016; Li et al., 2017a), did not take into account the misregistration between the sensors (Flood, 2017), considered TOA reflectance for desert sites only (Li et al., 2017a), used atmospherically corrected data but without image specific aerosol optical depth retrievals (Flood, 2017; Mandanici and Bitelli, 2016), used simulated reflectance data only (Gorroño et al., 2017) or did not consider a large amount of data (Mandanici and Bitelli, 2016; Li et al., 2017a).

The paper is structured as follows. First, the satellite data and pre-processing required to allow their meaningful comparison are described, and then the analysis methodology and results are described. The spectral band and NDVI transformations are provided so that the user community may use them to make Landsat-8 OLI and Sentinel-2A MSI data more consistent with each other. This is followed by concluding remarks with implications and recommendations.

2. Data

2.1. Sentinel-2A and Landsat-8 data

The Sentinel-2A, launched in June 2015, carries the Multi Spectral Instrument (MSI) that has a 10-day repeat cycle over a 290-km-wide swath (Drusch et al., 2012). The Landsat-8 satellite, launched in February 2013, carries the OLI and Thermal Infrared Sensor (TIRS) that sense the Earth's land surface with a 16 day repeat cycle over a 185-km-wide swath (Irons et al., 2012; Loveland and Irons, 2016). Combination of the data from these two sun-synchronous polar orbiting systems provides a global median average revisit interval of 4.6 days (Li and Roy, 2017). Both sensors have 12-bit radiometric resolution providing high dynamic range and also infrequent band saturation over highly reflective surfaces. The Landsat-8 OLI and Sentinel-2A MSI on orbit reflective wavelength calibration is better than 3% (Markham et al., 2014; Mishra et al., 2016; Gascon et al., 2017). The Sentinel-2A MSI has 13 reflective wavelength bands; four 10 m visible and near-infrared (NIR) bands, six 20 m red edge, near-infrared and short wave infrared (SWIR) bands, and three 60 m bands (Drusch et al., 2012). The Landsat-8 OLI has 9 reflective wavelength bands with six of them (blue, green, red, NIR, SWIR-1, SWIR-2) designed for land applications at the Landsat heritage 30 m spatial resolution (Irons et al., 2012). Each of the six Landsat-8 OLI bands (Fig. 1) has a corresponding Sentinel-2A MSI wavelength band, and there are two Sentinel-2 MSI NIR bands that are defined at 10 m (115 nm wide) and 20 m (20 nm wide). In this study these different sensor bands (Table 1) were compared.

Sentinel-2A has a 20.6° field of view and senses a 290 km swath. The data are provided as TOA reflectance in 109×109 km L1C tiles in the

Universal Transverse Mercator (UTM) map projection (ESA (European Space Agency), 2015). Adjacent L1C tiles in the same UTM zone from the same swath overlap by about 10 km, and adjacent tiles from the same MSI swath may be defined in different UTM zones (Roy et al., 2016c). The L1C cloud mask product is not currently reliable. Consequently, in this study the cloud mask and per-pixel quality information generated by the Sentinel-2 radiative transfer atmospheric correction code SEN2COR (Müller-Wilm, 2016) was used.

Landsat-8 has a 15° field-of-view and senses a 185 km swath. The data are defined in 185×185 km images in the World-wide Reference System (WRS-2) path (ground track parallel) and row (latitude parallel) coordinates (Arvidson et al., 2001). The Landsat archive was re-processed into a tiered data Collection structure in 2017. In this study, Landsat-8 Collection 1 Level 1 Precision and Terrain (L1TP) corrected data were used. The Collection 1 data provide a number of new metadata, including angle coefficients that may be used to derive per-pixel solar and viewing geometry, and also provide per-pixel cloud, cloud shadow, cirrus cloud and snow masks derived from the CFmask algorithm (Foga et al., 2017).

2.2. Study area and time period

Fig. 2 illustrates the study area that corresponds to the area defined by MODIS land tile h20v10 (Wolfe et al., 1998) and covers approximately 1200×1200 km over southern Africa centered on western Zambia. The study area was classified by the Collection 5500 m MODIS land cover product (Friedl et al., 2010) as predominantly savanna (49.0%), woody savanna (42.5%), and grassland (1.7%). The other International Geosphere-Biosphere Program (IGBP) classes were present in smaller amounts except for the evergreen needleleaf, snow and ice classes. Fig. 2 shows a four day period of Sentinel-2A MSI (left) and Landsat-8 OLI (right) acquisitions processed as described below (Section 3.2). A greater surface area is observed per unit time by Sentinel-2A compared to Landsat-8. This is because Sentinel-2A has a shorter revisit cycle and a wider field of view and also because different orbits of Sentinel-2A data laterally overlap at these latitudes every 3 and 7 days whereas different orbits of Landsat-8 data laterally overlap every 7 and 9 days.

To ensure that a representative range of reflectance spectra were considered, all the available Landsat-8 OLI Collection 1 L1TP and Sentinel-2A L1C data over the study area for two summer (December and January) and two winter (June and July) months, 2016 were considered. A total of 209 and 255 Landsat-8 L1TP images and 1545 and 1687 Sentinel-2A L1C tile acquisitions were available in the summer and winter months respectively. There were less summer data because of greater cloud cover that reduced the number of Landsat images processed to L1TP and because in a summer month, i.e., January, the Sentinel-2A Commissioning Phase was still ongoing and so Sentinel-2A data were generally less available. These southern hemisphere winter and summer months capture senescent dry vegetation (June and July) and green leaf-on vegetation (December and January) conditions, respectively, and are likely to have different surface moisture and atmospheric conditions. The average winter two month data solar zenith was 46.37° (Sentinel-2A 45.10° and Landsat-8 47.64°) and the average summer two month data solar zenith was 32.12° (Sentinel-2A 30.38° and Landsat-8 33.87°).

3. Data pre-processing

3.1. Reflectance simulation by convolution of sensor spectral response functions with library spectra

To gain insights into any reflectance differences between the two sensors due only to their spectral resolution differences (Fig. 1) a large number of simulated sensor reflectance values were generated. Sentinel-2A MSI and Landsat-8 OLI band reflectance values were derived

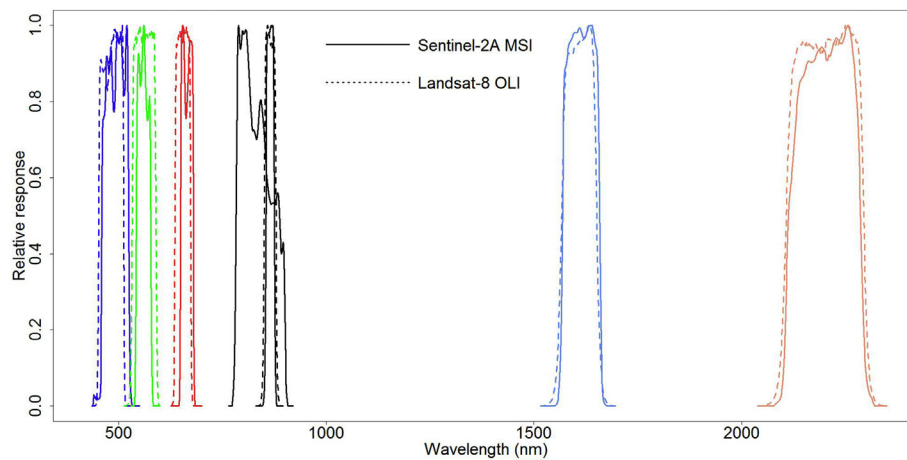


Fig. 1. Spectral response functions for the approximately equivalent Sentinel-2A MSI (solid lines) and Landsat-8 OLI (dashed lines) for the bands used in this research (Table 1). Spectral response functions obtained from <https://sentinel.esa.int/web/sentinel/user-guides/document-library> (version 3.0 released December 19th 2017) and <https://landsat.usgs.gov/using-usgs-spectral-viewer>.

by convolving laboratory spectra with sensor-specific spectral response functions (Steven et al., 2003; Zhang and Roy, 2016a) as:

$$\bar{\rho}_{band} = \frac{\int_{band_{\lambda_{min}}}^{band_{\lambda_{max}}} s_{band}(\lambda) \rho(\lambda) d\lambda}{\int_{band_{\lambda_{min}}}^{band_{\lambda_{max}}} s_{band}(\lambda) d\lambda} \quad (1)$$

where $\bar{\rho}_{band}$ is the simulated reflectance for a specific Sentinel-2 or Landsat-8 band (Table 1), $s_{band}(\lambda)$ is the Sentinel-2A or Landsat-8 spectral response function for the band (Fig. 1), and $band_{\lambda_{min}}$ and $band_{\lambda_{max}}$ are the minimum and maximum wavelengths where $s_{band}(\lambda)$ is greater than zero, and $\rho(\lambda)$ is the spectral library data for a given spectrum. A total of 485 spectra were used: 224 vegetation, 40 soil, 147 man-made materials, and 74 dry vegetation spectra. The spectra are extracted from three spectral libraries: the Version 6 USGS spectral library (Clark et al., 2007), the Version 2 ASTER spectral library (Baldrige et al., 2009), and the Jasper Ridge spectral library (ENVI, 2013). The simulated normalized difference vegetation index (NDVI) was derived as the simulated NIR reflectance minus the simulated red reflectance divided by their sum. There are two Sentinel-2A MSI NIR bands and throughout the paper the Sentinel-2A NDVI was always derived using the narrower MSI NIR band 8A (855–875 nm) as it is more comparable to the Landsat-8 OLI NIR band 5 (851–879 nm) (Table 1, Fig. 1).

3.2. Sentinel-2A and Landsat-8 data pre-processing

3.2.1. Top of atmosphere reflectance and geometry derivation

The Landsat-8 Collection 1 L1TP digital numbers for each band were converted to top of atmosphere (TOA) reflectance using the scaling factors stored in the metadata and dividing by the cosine of the solar zenith angle. Landsat per-pixel solar and viewing angles were calculated using the Landsat Angles Creation Tool provided by USGS (<https://landsat.usgs.gov/solar-illumination-and-sensor-viewing-angle-coefficient-file>) and the angle coefficient file available with each

Collection 1 L1TP file. The Sentinel-2A L1C tile data store the TOA reflectance, and also the solar and view geometry every 5 km. The Sentinel-2A solar and view zenith angles were bilinear resampled to provide angles for each Sentinel-2A pixel location.

3.2.2. Surface reflectance computation

The Sentinel-2A and Landsat-8 sensor TOA reflectance data were corrected to surface reflectance using the same algorithm to reduce biases that may occur if different algorithms were used. The LaSRC (Land Surface Reflectance Code) algorithm V3.5.5 (Vermote et al., 2016), that has been adapted for Sentinel-2A application, was used in this study. The LaSRC has higher accuracy than the heritage LEDAPS algorithm (Masek et al., 2006) when applied to Landsat-8 OLI data (Vermote et al., 2016). It is based on the established 6S radiative transfer code (Vermote et al., 1997) with, in particular, an improved aerosol determination based on a red to blue reflectance ratio and a linear function of a spectral index with slope and intercept terms derived from a spatially explicit climatology of MODIS and MISR data.

3.2.3. Nadir BRDF-adjusted reflectance (NBAR) computation

Most land surfaces do not have a Lambertian BRDF and so reflectance may vary due only to variations in the solar and viewing geometry. Across the Landsat swath the red and NIR reflectance can vary by up to 0.02 and 0.06 (reflectance units) due only to BRDF effects (Roy et al., 2016a) and by up to 0.06 and 0.08 for Sentinel-2A because of its wider field of view (Roy et al., 2017). These differences may constitute a significant source of noise for many applications as they are comparable and greater than the sensor calibration errors (Mishra et al., 2016; Gascon et al., 2017). A semi-physical approach developed for Landsat application (Roy et al., 2016a) and demonstrated to also work for Sentinel-2A (Roy et al., 2017) was used to adjust the surface reflectance for each sensor band to a nadir view (0° view zenith) and the observed solar zenith angle.

Table 1

The Sentinel-2A MSI and Landsat-8 OLI approximately equivalent spectral bands (Drusch et al., 2012; Barsi et al., 2014) considered in this study.

Sentinel-2A MSI			Landsat-8 OLI		
Band	Resolution (m)	Wavelength Range (nm)	Band	Resolution (m)	Wavelength Range (nm)
B2 (blue)	10	458–523	B2	30	452–512
B3 (green)	10	543–578	B3	30	533–590
B4 (red)	10	650–680	B4	30	636–673
B8 (NIR)	10	785–900	B5	30	851–879
B8A (NIR)	20	855–875			
B11 (SWIR-1)	20	1565–1655	B6	30	1566–1651
B12 (SWIR-2)	20	2100–2280	B7	30	2107–2294

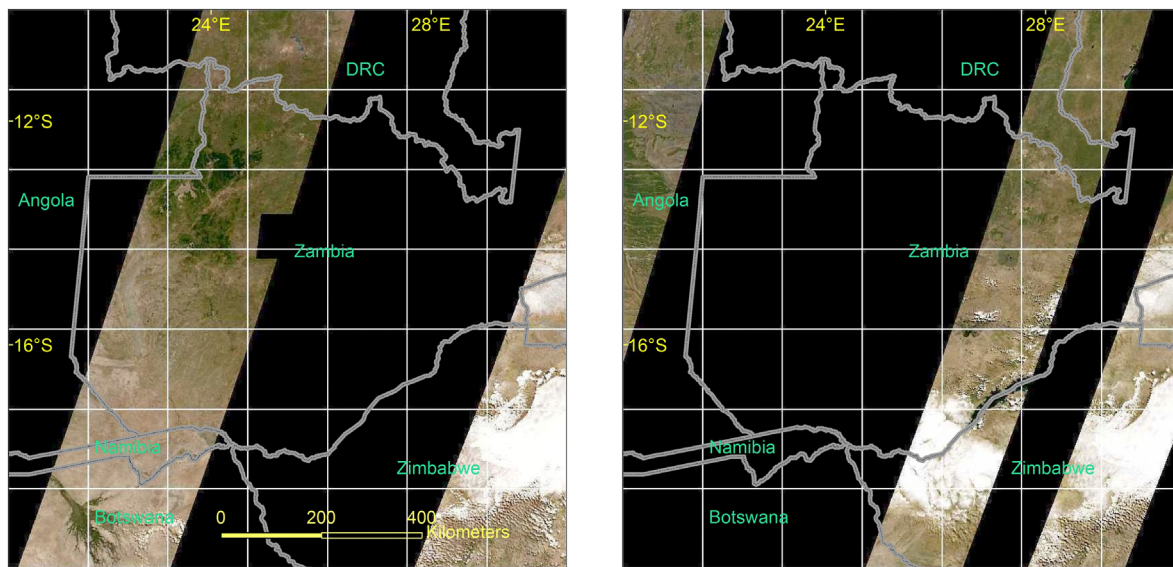


Fig. 2. Study area over southern Africa corresponding to $10^{\circ} \times 10^{\circ}$ MODIS land tile (h20v10) showing Sentinel-2A MSI (left) and Landsat-8 OLI (right) true color surface NBAR for four days, July 14 to 18 2016. The white lines show the boundaries of 49 sinusoidal 5295×5295 30 m pixel tile boundaries. The atmospheric correction was undertaken using the LaSRC (Land Surface Reflectance Code) (Vermote et al., 2016) and the data were adjusted to NBAR using the c-factor method (Roy et al., 2016a, 2017). (For interpretation of the references to color in this figure legend, the reader is referred to the web version of this article.)

3.2.4. Cloud, cloud shadow and spectral saturation masking

Clouds, shadows and saturation preclude meaningful surface observation at reflective wavelengths. Given the large amount of data considered in this study, contaminated or potentially contaminated Sentinel-2A and Landsat-8 observations were aggressively removed to ensure meaningful sensor comparison.

The Sentinel-2A L1C cloud mask product is not currently reliable. Consequently, in this study, as in Roy et al. (2017), the cloud and shadow mask generated by the Sentinel-2 radiative transfer atmospheric correction code SEN2COR (Version 2.3.1, February 2017 release) (Müller-Wilm, 2016) was used. The SEN2COR uses a set of spectral reflectance rules based on the established Landsat automatic cloud cover assessment algorithm (ACCA) (Irish et al., 2006) to derive a 20 m cloud mask. It then applies spectral reflectance rules combined with a cloud shadow probability derived from an a priori cloud height distribution with the sun-sensor-cloud geometry to label 20 m cloud shadow pixels (Richter et al., 2012). In this study, any 20 m pixels labeled by SEN2COR as saturated, medium or high confidence cloud, cloud shadow, snow, or cirrus were discarded.

The Landsat-8 Collection 1 L1TP product includes a per-pixel bit-packed quality band (Foga et al., 2017). Pixels labeled as medium or high confidence cloud, cloud shadow, cirrus, or snow were all discarded. Landsat-8 reflective wavelength data are much less saturated compared to previous Landsat's (Roy et al., 2016b) but if any of the six Landsat-8 bands (Table 1) were labeled as saturated then the pixel observation was discarded. The saturation status was derived by comparison of the stored digital numbers and metadata saturation values.

Medium resolution satellite data may have pronounced adjacency effects whereby atmospheric scattering from adjacent pixel locations may contribute non-negligible scattered radiation into the sensed pixel (Ouaidrari and Vermote, 1999; Liang et al., 2001; Houborg and McCabe, 2017). In particular, adjacency effects near clouds can be pronounced (Marshak et al., 2008; Tackett and Di Girolamo, 2009). To reduce adjacency effects, any Landsat-8 or Sentinel-2A pixel directly next to a cloud, cirrus or cloud shadow was discarded.

3.2.5. Registration, reprojection, and tiling

Sentinel-2A and Landsat-8 data are currently not well registered (Yan et al., 2016; Storey et al., 2016; Gascon et al., 2017; Skakun et al., 2017). In this study the data were registered to sub-pixel precision

using an image pyramid area and feature based matching algorithm applied to the MSI 10 m NIR band and OLI 30 m NIR band resampled to 10 m (Yan et al., 2016). A least-squares adjustment was applied to matched points derived among acquisitions sensed by different orbits (Yan et al., 2018). Each Sentinel-2A and Landsat-8 acquisition was reprojected into 5295×5295 30 m pixel non-overlapping tiles defined in the equal-area sinusoidal map projection (e.g., Fig. 2). Specifically, each 30 m pixel location (sinusoidal coordinates) across the tile was projected into the Sentinel-2 L1C data, taking care to use the correct L1C tile UTM zone (Roy et al., 2016c), and also projected into the Landsat-8 Collection 1 data. Each orbit of satellite data was reprojected and stored independently so no temporal compositing was undertaken. The affine transformations defined by the least-squares registration characterization were injected into the sinusoidal to UTM coordinate transformation so that the satellite data were not resampled twice. The Sentinel-2A 20 m and the Landsat-8 30 m band data were resampled by bilinear resampling. The Sentinel-2A 10 m bands were resampled using a box-car resampler, whereby the four corners of each sinusoidal projection 30 m pixel were projected into the Sentinel-2A UTM projection and all the 10 m Sentinel-2A pixels intersecting the projected pixel were identified and their average reflectance used as the resampled value.

4. Landsat-8 OLI and Sentinel-2 MSI reflectance comparison methodology

4.1. Simulated spectral reflectance and NDVI sensor comparison

The Sentinel-2A MSI and Landsat-8 OLI spectral response functions are quite different (Fig. 1). To examine the impact of this, scatterplots of simulated MSI against simulated OLI sensor reflectance (Eq. (1)) were generated for each of the approximately equivalent sensor bands and also for the derived NDVI. The degree of correspondence between the sensor data was examined by reduced major axis (RMA) regression that allows for both the dependent and independent variables to have comparable error and means that swapping the dependent and independent variables (i.e., the Sentinel-2A and Landsat-8 band data) will not alter the bivariate relationship (Smith, 2009). The RMA regression was set with an intercept of zero as no systematic biases are expected or are modeled by Eq. (1). In addition, the root mean square difference between the Sentinel-2A and Landsat-8 simulated data was derived as:

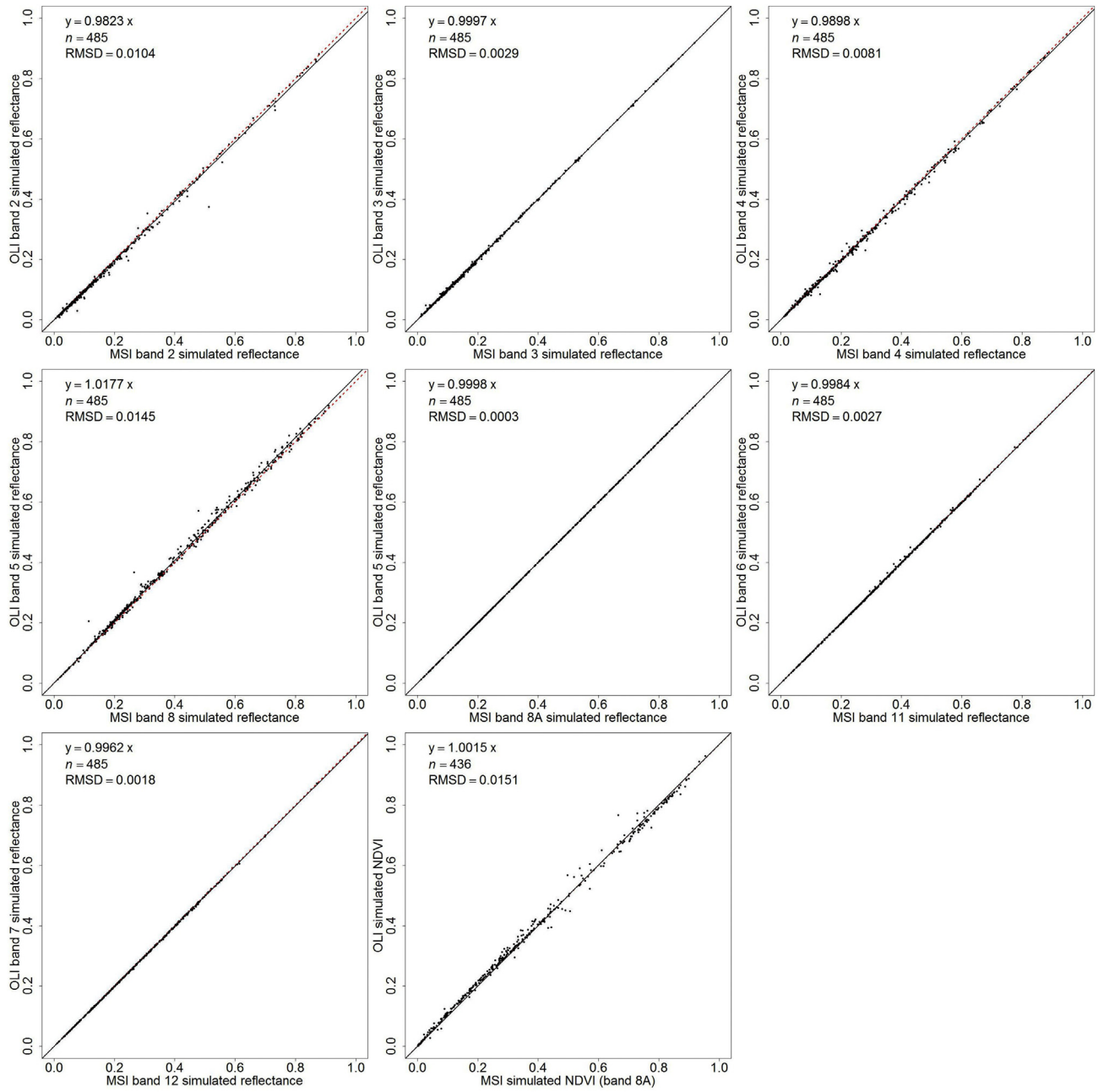


Fig. 3. Simulated spectral reflectance and simulated NDVI fitted using the reduced major axis (RMA) regression (solid black lines) without intercept. The red dotted lines are 1:1 lines superimposed for reference. The root mean square difference (RMSD) is calculated as Eq. (2). Only NDVI values in the range 0.0 to 1.0 are illustrated providing fewer (436) simulated NDVI values. (For interpretation of the references to color in this figure legend, the reader is referred to the web version of this article.)

$$RMSD = \sqrt{\frac{\sum_{i=1}^n (v_i^{OLI} - v_i^{MSI})^2}{n}} \quad (2)$$

where RMSD is the root mean square difference between corresponding Landsat-8 OLI (v_i^{OLI}) and Sentinel-2A MSI (v_i^{MSI}) simulated reflectance or NDVI values derived as Eq. (1) for spectra i , and there are $n = 485$ spectra.

4.2. Sentinel-2A MSI and Landsat-8 OLI spectral reflectance and NDVI sensor comparison

To generate data for the analysis, pixels were sampled systematically every five 30 m pixels in the row and column directions across

each Sentinel-2A and Landsat-8 5295 × 5295 30 m pixel tile for each orbit of reprojected data. Only pairs of Sentinel-2A and Landsat-8 pixel observations that were both valid, i.e., not cloudy, shadow, or cirrus contaminated (Section 3.2.4) were compared. Only pairs of Sentinel-2A and Landsat-8 pixel observations acquired within one-day of each other were considered to minimize the impact of surface changes between the MSI and OLI sensor observations. In addition, following the approach used to quantify spectral relationships between Landsat-7 Enhanced Thematic Plus and Landsat-8 OLI data sensed one day apart (Roy et al., 2016b), a blue band TOA reflectance filter was applied to reject pairs of Sentinel-2A and Landsat-8 pixel observations if:

$$\frac{|\rho_{blue}^{TOA,MSI} - \rho_{blue}^{TOA,OLI}|}{0.5 |\rho_{blue}^{TOA,MSI} + \rho_{blue}^{TOA,OLI}|} > 1.0 \quad (3)$$

where $\rho_{\text{blue}}^{\text{TOA, MSI}}$ is the TOA MSI band 2 (458–523 nm) reflectance and $\rho_{\text{blue}}^{\text{TOA, OLI}}$ is the TOA OLI band 2 (452–512 nm) reflectance. This filter will reject pairs of observations where the atmosphere changes considerably and is used because the blue band is most sensitive to atmospheric effects (Ju et al., 2012). It will also tend to reject pairs of observations if one of the two observations is cloud or snow covered as vegetation and soil typically have considerably lower blue reflectance than cloud or snow (Hagolle et al., 2010; Ustin et al., 1998). A minority of atmospherically corrected observations may have abnormal values (reflectance greater than one or less than zero) due primarily to “over correction” by the atmospheric correction (Roy et al., 2014b) and so these observations were removed from the surface reflectance and surface NBAR comparisons.

Comparisons of the TOA reflectance, surface reflectance, surface NBAR, and derived NDVI were undertaken. For the NDVI comparisons, only NDVI values falling in the range zero to unity were retained to reflect typical land surface NDVI values. The correspondence between the comparable Sentinel-2A MSI and Landsat-8 OLI sensor band data were examined in the same way as for the simulated data, i.e., by RMA regression. In addition, to provide other overall summary difference measures that capture the directionality of any differences, the mean difference and the mean relative difference between the Landsat-8 and Sentinel-2A data were derived as:

$$\bar{\Delta} = \sum_i^n \frac{v_i^{\text{OLI}} - v_i^{\text{MSI}}}{n} \quad (4)$$

$$\bar{\Delta}^* = \frac{\sum_i^n \left((v_i^{\text{OLI}} - v_i^{\text{MSI}}) / 0.5(v_i^{\text{OLI}} + v_i^{\text{MSI}}) \right)}{n} 100 \quad (5)$$

where $\bar{\Delta}$ and $\bar{\Delta}^*$ are the mean difference and the mean relative difference respectively between corresponding Landsat-8 OLI (v_i^{OLI}) and Sentinel-2A MSI (v_i^{MSI}) values (TOA reflectance, surface spectral reflectance, surface NBAR, or derived NDVI) for n pairs of sensor observations.

Statistical functions to transform between the Sentinel-2A MSI and Landsat-8 OLI data (TOA reflectance, surface spectral reflectance, surface NBAR, and derived NDVI) were developed using ordinary least squares (OLS) regression. The goodness of fit of the OLS regressions were defined by the coefficient of determination (r^2) and the significance of the OLS regressions was defined by examination of the regression overall F-statistic p -value.

5. Results

5.1. Simulated spectral reflectance and NDVI sensor comparison

Fig. 3 shows scatter plots of the simulated Sentinel-2A MSI and Landsat-8 OLI reflectance for the approximately equivalent sensor spectral bands and the derived NDVI. The spectra used in this study provide simulated values that fall over a wide range of reflectance and NDVI but are located around the 1:1 line (the red dotted lines). For all of the bands, except the MSI broad and OLI NIR bands, the RMA slopes are less than unity (0.9823 to 0.9998), i.e., in general the Sentinel-2A MSI simulated reflectance is greater than the simulated Landsat-8 OLI reflectance.

The RMSD values are quite small (< 0.015) for all of the reflective bands. The greatest reflective band difference is between the MSI NIR broad band 8 (785–900 nm) and the Landsat-8 OLI NIR band 5 (851–879 nm) (RMSD = 0.0145). This is expected and is because these two bands have very different bandwidths - the OLI band 5 NIR spectral response function intersects with only 21.2% of the MSI NIR band 8 response function (Fig. 1). The RMA slope for this pair of bands is 1.0177, i.e., in general the simulated MSI NIR broad band reflectance is smaller than the simulated Landsat-8 OLI NIR reflectance. When the MSI NIR narrow band 8A (855–875 nm) is compared with the Landsat-8

OLI NIR band 5 the difference is less pronounced (RMSD = 0.0003) and the RMA slope is very close to unity (0.9998).

The simulated NDVI data have an RMA slope close to unity (1.0015). However, the NDVI RMSD is not negligible (0.0151). The NDVI is designed to emphasize the difference between red and NIR reflectance to differentiate between vegetation and soil. The red (RMSD 0.0081) and NIR (RMSD 0.0003) simulated reflectance differences are propagated into the NDVI differences that are larger than either band alone which is expected from NDVI spectral band propagation analyses (Miura et al., 2000).

The sensor differences illustrated in Fig. 3 are due only to simulated spectral response function differences. The simulation assumed implicitly that the surface was homogeneous with lambertian reflectance, and that there were no calibration or geolocation errors, and no atmospheric scattering or absorption, residual clouds or shadows. This is not the case for actual MSI and OLI data that are examined in the following section.

5.2. Spectral reflectance and NDVI sensor comparison

5.2.1. Data sampling

Over the study area there were 464 Landsat-8 Collection 1 L1TP images and 3232 Sentinel-2A L1C tile acquisitions available in the summer (December and January) and the winter (June and July) 2016. From these, 206 Landsat-8 OLI images and 707 Sentinel-2A L1C tile acquisitions were acquired within one day of each other. From these, pairs of MSI and OLI 30 m pixel observations were extracted across the tiles (Fig. 1) every five 30 m pixels. This sampling was necessary to reduce the data volume, and even so, a total of 116,164,813 pairs of MSI and OLI 30 m pixel observations were extracted. After filtering to remove saturated, cloud, cloud shadow, cirrus and snow contaminated pixels 65,380,881 pairs remained. The blue TOA reflectance filter (Eq. (3)) removed a very small number of pairs (29) and consequently 65,380,852 pixels were used for the TOA analyses. The atmospheric correction resulted in a minority of over-corrected reflectance values (i.e., values less than zero or greater than unity) and these were removed from the surface reflectance and from the surface NBAR analyses. The over correction varied among bands but occurred more frequently for the shorter wavelength bands ($< 0.1\%$ removed) than for the longer wavelength bands ($< 0.002\%$ removed). For all the analyses about 65 million pairs of Sentinel-2A MSI and Landsat-8 OLI 30 m pixel observations were considered.

5.2.2. Top of atmosphere spectral reflectance and NDVI sensor comparison

Fig. 4 shows scatter plots of the Sentinel-2A MSI and Landsat-8 OLI TOA reflectance for the approximately equivalent sensor spectral bands and the derived TOA NDVI. The range of the MSI and OLI values indicates a considerable spectral variation in the surface type and condition across the study area and for the winter and summer months. If there was no difference between the MSI and OLI sensor data then all of the plotted data would fall on the 1:1 line (dashed) and the OLS regressions of MSI against OLI (green lines) and of OLI against MSI (blue lines) and the RMA regressions (black lines) would have slopes of unity and zero intercepts. Departures from the 1:1 line could be due to several confounding factors including spectral band pass difference (as illustrated in Fig. 3) but also atmospheric contamination, calibration, and bi-directional reflectance differences. These are examined and discussed in the following sections.

The solid lines in Fig. 4 show the RMA regressions derived without intercept and so are directly comparable to the simulated RMA regression results illustrated in Fig. 3. As for the simulated data, the RMA TOA reflectance slopes are in general less than unity, i.e., the MSI TOA reflectance is greater than the OLI TOA reflectance, but with slopes that are further from unity likely due to the confounding factors noted above. The exceptions are the blue and broad band NIR TOA reflectance data. The blue band (MSI band 2 and OLI band 2) data have an RMA

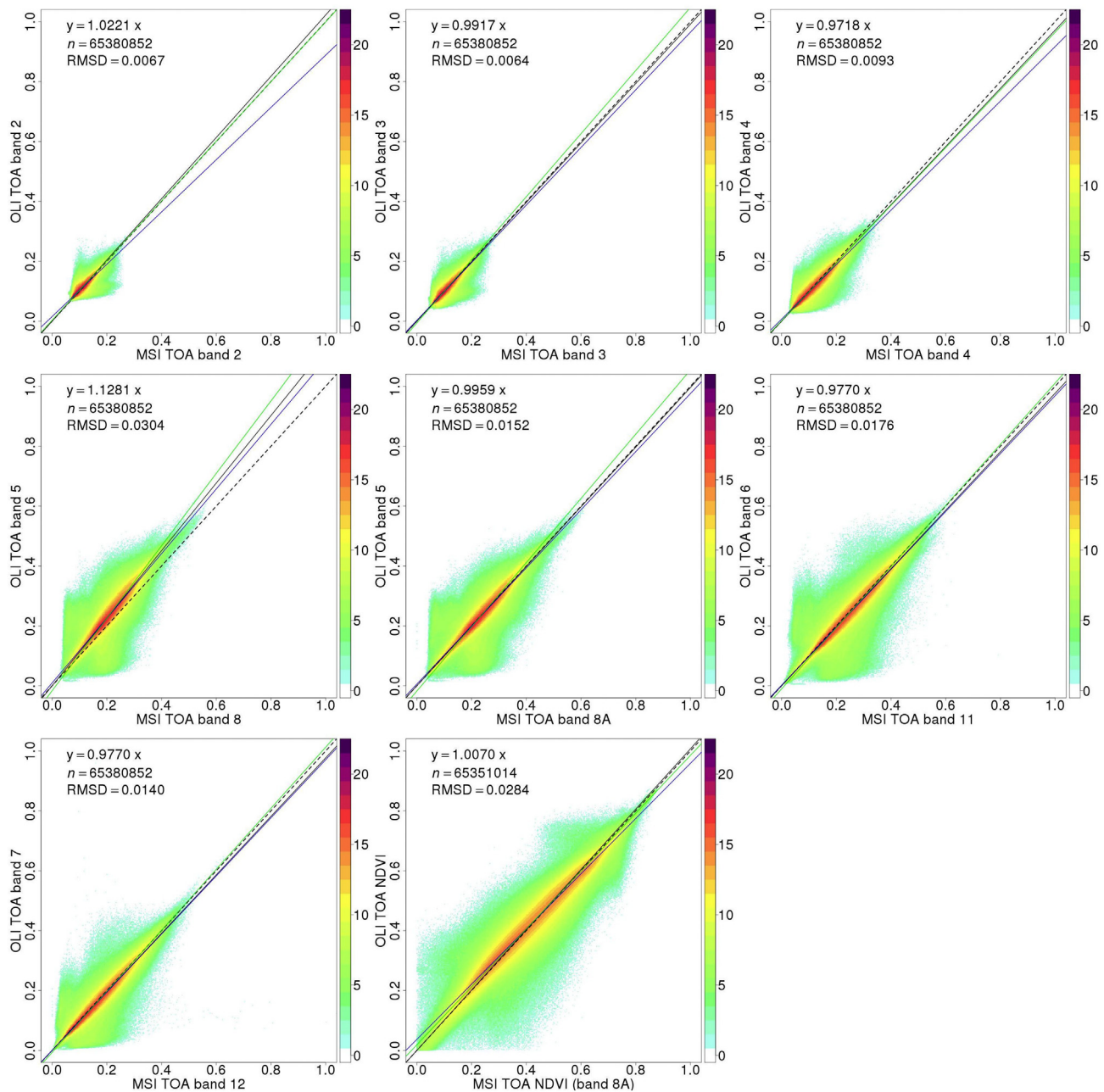


Fig. 4. Scatter plot of the Sentinel-2A and Landsat-8 TOA spectral reflectance and NDVI. The black lines are fitted using the reduced major axis (RMA) regression with equations shown in the top left, the blue lines show ordinary least squares (OLS) regression of the OLI against the MSI data, and the green lines show OLS regression of the MSI data against the OLI data. Only NDVI values in the range 0.0 to 1.0 are illustrated. The dotted lines are 1:1 lines superimposed for reference. The plot colors show the frequency of occurrence of similar error values with a log2 scale. (For interpretation of the references to color in this figure legend, the reader is referred to the web version of this article.)

slope of 1.0221 (compared to 0.9823 for the simulated data) and is the shortest wavelength band considered and so is more susceptible to atmospheric effects present in the TOA data than the longer wavelength bands. The broad band NIR (MSI band 8 and OLI band 5) TOA RMA slope is larger than unity (1.1281) and further from unity than for the simulated data (1.0177) for the reasons described in the following paragraph. The TOA NDVI RMA slope (1.0070) is greater than the simulated NDVI slope (1.0015, Fig. 3), i.e., the MSI TOA NDVI is generally smaller than the OLI TOA NDVI.

Table 2 summarizes the OLS regressions, the mean difference ($\bar{\Delta}$, Eq. (4)) and the mean relative difference ($\bar{\Delta}^*$, Eq. (5)) statistics between the two sensor data. The OLS regression r^2 values are all > 0.87 and are highly significant (p -values < 0.0001) indicating that the regression

parameters can be used to transform TOA reflectance or TOA NDVI between the two sensors. All of the OLS reflectance slopes fall in the range 0.9103 to 1.0378 except for the blue (MSI band 2 and OLI band 2) and broad band NIR (MSI band 8 and OLI band 5). These exceptions are likely related to atmospheric effects. The MSI and OLI blue bands are the shortest wavelengths bands considered in this study and so are the most sensitive to aerosol and molecular scattering (Ju et al., 2012; Hagolle et al., 2015; Vermote et al., 2016). The MSI broad band NIR (MSI band 8) includes water absorption wavelengths (Kaufman and Gao, 1992) that were purposefully avoided by the OLI NIR band design (Irons et al., 2012).

The MSI and OLI TOA reflectance mean relative differences are generally comparable in magnitude to the Landsat-8 OLI and Sentinel-

Table 2

Sentinel-2A MSI and Landsat-8 OLI TOA reflectance and TOA NDVI sensor transformation functions for the approximately equivalent spectral bands (Table 1) derived by ordinary least squares (OLS) regression of the data illustrated in Fig. 4. The number of pairs of sensor values considered (n), the regression coefficient of determination (r^2) and F-test p -value, and the mean difference (Eq. (4)) and mean relative difference (Eq. (5)) between the OLI and MSI data are tabulated.

	Between sensor OLS transformation functions and regression coefficients	n	OLS r^2 (p -value)	Mean OLI – MSI difference ($\bar{\Delta}$) (units: reflectance 0–1, or NDVI 0–1)	Mean relative OLI – MSI difference ($\bar{\Delta}^*$) (units: %)
Blue λ (~0.48 μm)	OLI = 0.0154 + 0.8729 MSI MSI = -0.0029 + 1.0036 OLI	65,380,852	0.8761 (< 0.0001)	0.0025	2.67
Green λ (~0.56 μm)	OLI = 0.0027 + 0.9621 MSI MSI = 0.0056 + 0.9496 OLI	65,380,852	0.9136 (< 0.0001)	-0.0009	-0.99
Red λ (~0.66 μm)	OLI = 0.0066 + 0.9103 MSI MSI = -0.0014 + 1.0378 OLI	65,380,852	0.9447 (< 0.0001)	-0.0023	-1.67
Near infrared λ (~0.85 μm) MSI Band 8	OLI = 0.0096 + 1.0794 MSI MSI = 0.0136 + 0.8268 OLI	65,380,852	0.8924 (< 0.0001)	0.0255	11.89
Near infrared λ (~0.85 μm) MSI Band 8A	OLI = 0.0056 + 0.9701 MSI MSI = 0.0163 + 0.9331 OLI	65,380,852	0.9052 (< 0.0001)	-0.0012	-0.62
Shortwave infrared λ (~1.61 μm)	OLI = 0.0019 + 0.9668 MSI MSI = 0.0102 + 0.9795 OLI	65,380,852	0.9470 (< 0.0001)	-0.0056	-2.66
Shortwave infrared λ (~2.21 μm)	OLI = 0.0005 + 0.9702 MSI MSI = 0.0063 + 0.9815 OLI	65,380,852	0.9523 (< 0.0001)	-0.0038	-2.93
NDVI	OLI = 0.0369 + 0.9218 MSI MSI = -0.0195 + 1.0348 OLI	65,351,014	0.9538 (< 0.0001)	0.0053	1.96

2A MSI on orbit calibration performances of better than 3% (Markham et al., 2014; Gascon et al., 2017). The MSI and OLI TOA reflectance data have small mean differences ($|\bar{\Delta}| < 0.006$) and mean relative differences ($\bar{\Delta}^* < 3\%$) for all of the TOA reflectance bands except the broad band MSI NIR band comparison. The broad band MSI NIR band reflectance is quite different to the OLI NIR band ($\bar{\Delta} = 0.0255$ and $\bar{\Delta}^* = 11.89\%$) and this is likely due to their different band passes as noted in Section 5.1 and the susceptibility of the broad band MSI NIR band to atmospheric effects as noted above. The TOA NDVI MSI and OLI data are also similar ($\bar{\Delta} = 0.0053$ and $\bar{\Delta}^* = 1.96\%$).

5.2.3. Atmospherically corrected spectral reflectance and NDVI sensor comparison

Fig. 5 shows the atmospherically corrected results, i.e., the differences between the MSI and OLI surface reflectance and surface NDVI data. The atmospheric correction increases the data range, particularly for the visible reflectance bands and the NDVI (Fig. 5 compared to Fig. 4). This has been seen in similar studies (Roy et al., 2014b, 2016b) and occurs because atmosphere contamination generally reduces the surface contrast due to Rayleigh and aerosol backscatter that contribute positively to the sensor signal over dark surfaces and aerosol absorption that reduces the sensor signal over bright surfaces (Tanre et al., 1981). The surface reflectance RMA regression slopes changed significantly (> 0.02) for the visible and broad band NIR comparisons compared to the TOA reflectance regressions which is likely due to the susceptibility of these bands to atmospheric contamination. There is little difference between the TOA and surface reflectance RMA slopes for the other bands, or for NDVI, and the largest difference is for the green band which has an RMA slope of 1.0572 (surface reflectance) and 0.9917 (TOA reflectance).

Table 3 summarizes the surface reflectance and surface NDVI OLS regressions and difference statistics between the MSI and OLI data. The OLS r^2 values are all > 0.89 and highly significant (p -values < 0.0001). The atmospheric correction improves the goodness of fit of the OLS regressions between the MSI and OLI reflectance data with greater r^2 values for the surface blue, green, and broad band NIR, and NDVI data (Table 3) compared to the TOA equivalents (Table 2). The surface reflectance (Fig. 5) and TOA reflectance (Fig. 4) OLS regression slopes are quite similar (within 2%), except for the blue, green, and broad NIR bands (MSI band 8 and OLI band 5) that are sensitive to atmospheric effects as described above. The surface NDVI and TOA NDVI OLS slopes

are marginally different ($< 4\%$).

The atmospheric correction increases the range in the reflectance and NDVI compared to the TOA results and so comparison of the TOA and surface mean difference ($\bar{\Delta}$) values in Tables 2 and 3 respectively is not particularly meaningful. The mean relative differences ($\bar{\Delta}^*$) can be compared however. The atmospheric correction reduces $\bar{\Delta}^*$ only for the red, both NIR bands and for the NDVI. The surface reflectance $\bar{\Delta}^*$ values are in particular much greater than the TOA reflectance $\bar{\Delta}^*$ values for the blue (surface reflectance $\bar{\Delta}^* = 4.64\%$) and green (surface reflectance $\bar{\Delta}^* = 4.80\%$) bands. This reflects the difficulty in reliably undertaking atmospheric correction at shorter wavelengths due primarily to aerosol characterization (Ju et al., 2012; Claverie et al., 2015; Hagolle et al., 2015). The longer wavelength ($\sim 2.21 \mu\text{m}$) SWIR band has similar $\bar{\Delta}^*$ for the TOA (-2.93%) and the surface reflectance (-2.95%) likely because atmospheric effects are minimal at this longest wavelength. The $\sim 1.62 \mu\text{m}$ SWIR band had greater surface reflectance $\bar{\Delta}^*$ (-3.56%) than for the TOA (-2.66%) and could be due to a LaSRC over-correction or a calibration issue in this band.

5.2.4. Atmospherically and BRDF corrected spectral reflectance and NDVI sensor comparison

Fig. 6 and Table 4 show the equivalent results as Fig. 5 and Table 3 but for the atmospherically and BRDF corrected data, referred to herein as surface NBAR and surface NBAR NDVI. Compared to the atmospherically corrected data (Fig. 5) the BRDF correction reduced the scatter in the data (Fig. 6) and the OLS r^2 values increased for all the reflective bands. This is consistent with previous findings that Landsat-8 OLI (Gao et al., 2014; Roy et al., 2016a) and Sentinel-2A MSI (Roy et al., 2017) reflectance are sensitive to viewing angle variations despite the relatively narrow sensor fields of view. In this study the solar zenith differences (MSI minus OLI) between the 65 million pairs of MSI and OLI observations were quite small (mean = -2.7199° , standard deviation = 0.7793° , range -5.82° to -0.87°) because the observations were acquired within one day of each other. The view zenith differences were much greater (mean = 1.2045° , standard deviation = 9.2581° , range -17.44° to 20.14° , where negative angles denote the forward scatter direction) and over non-lambertian surfaces cause non-negligible BRDF effects.

The surface NBAR NDVI regression slopes (RMA and OLS) (Fig. 6) are similar to the surface NDVI slopes (Fig. 5), and the OLS regression r^2 values are about the same. This is expected as to first order the NDVI

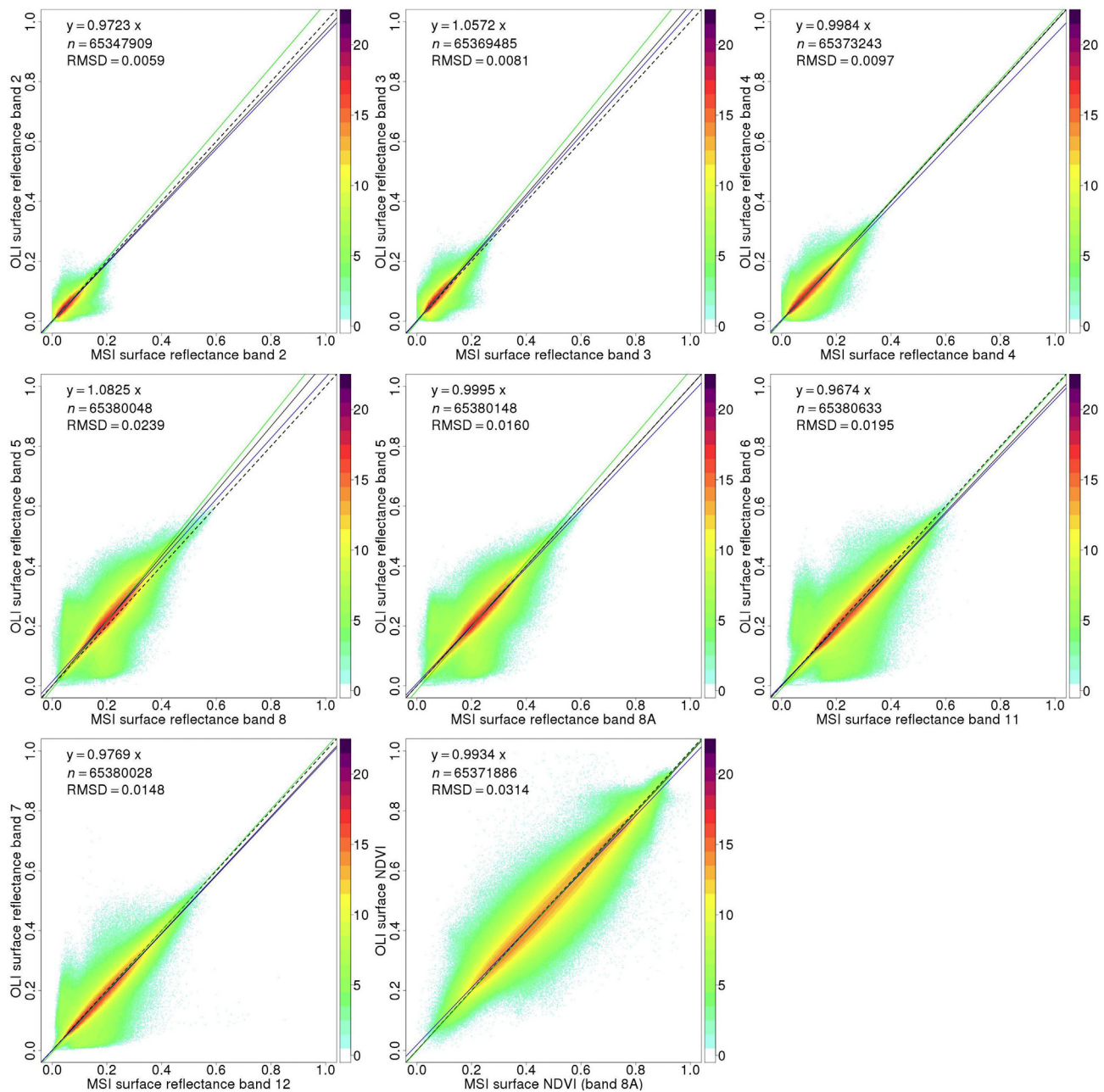


Fig. 5. As Fig. 4 but showing the atmospherically corrected data, i.e., surface reflectance and NDVI.

ratio formulation reduces sensitivity to BRDF effects compared to red and NIR reflectance (Gao et al., 2002). In addition, although BRDF effects occur in Landsat NDVI data due to solar zenith variations (Zhang and Roy, 2016b), they have less influence in this study given the small solar zenith differences between the MSI and OLI observations noted above.

The surface NBAR RMA regression slopes (Fig. 6) are always slightly lower than the surface reflectance RMA regression slopes (Fig. 5). Also, notably, the BRDF correction generally decreases the OLI against MSI OLS regression slopes (blue lines) and increases the MSI against OLI OLS regression slopes (green lines) compared to the atmospherically corrected data. The reasons for this are likely due to the greater view zenith angle range in Sentinel-2A MSI ($\pm 10.3^\circ$) compared to Landsat-8 OLI ($\pm 7.5^\circ$). Consequently, the MSI surface reflectance will change more than the OLI surface reflectance when corrected to NBAR. In addition, this may also be due to greater error in the BRDF correction with increasing view zenith. This is reasonable as the surface

reflectance anisotropy is corrected to NBAR by multiplying the surface reflectance with a c -factor defined as the ratio of reflectance values modeled using MODIS BRDF spectral model parameters for the observed and for a nadir view and the local solar zenith (Roy et al., 2016a, 2017).

The mean relative difference between the OLI and MSI bands ($\bar{\Delta}^*$) were smaller for the surface NBAR (Table 4) than for the surface reflectance (Table 3) green, red and broadband NIR comparisons. For the other bands, and the NDVI, the absolute value of the mean relative differences increased by $< 1.5\%$. The reasons for this are unresolved but these differences are quite small and could be due to numerous factors include those noted above.

6. Discussion and conclusion

The Sentinel-2 MSI and Landsat-8 OLI sensors have similar characteristics and their data together have the potential to support global

Table 3

Sentinel-2A MSI and Landsat-8 OLI surface reflectance and surface NDVI sensor transformation functions for the approximately equivalent spectral bands (Table 1) derived by ordinary least squares (OLS) regression of the data illustrated in Fig. 5. The number of pairs of sensor values considered (n), the regression coefficient of determination (r^2) and F-test p -value, and mean difference (Eq. (4)) and mean relative difference (Eq. (5)) between the OLI and MSI data are tabulated.

Between sensor OLS transformation functions and regression coefficients		n	OLS r^2 (p -value)	Mean OLI – MSI difference ($\bar{\Delta}$) (units: reflectance 0–1, or NDVI 0–1)	Mean relative OLI – MSI difference ($\bar{\Delta}^*$) (units: %)
Blue λ (~0.48 μm)	OLI = 0.0003 + 0.9570 MSI MSI = 0.0039 + 0.9383 OLI	65,347,909	0.8980 (< 0.0001)	–0.0014	–4.64
Green λ (~0.56 μm)	OLI = 0.0015 + 1.0304 MSI MSI = 0.0038 + 0.8909 OLI	65,369,485	0.9180 (< 0.0001)	0.0034	4.80
Red λ (~0.66 μm)	OLI = 0.0041 + 0.9533 MSI MSI = 0.0006 + 0.9902 OLI	65,373,243	0.9440 (< 0.0001)	0.0002	0.66
Near infrared λ (~0.85 μm) MSI Band 8	OLI = 0.0139 + 1.0157 MSI MSI = 0.0098 + 0.8795 OLI	65,380,048	0.8933 (< 0.0001)	0.0171	7.97
Near infrared λ (~0.85 μm) MSI Band 8A	OLI = 0.0077 + 0.9644 MSI MSI = 0.0147 + 0.9355 OLI	65,380,148	0.9022 (< 0.0001)	–0.0003	–0.22
Shortwave infrared λ (~1.61 μm)	OLI = 0.0034 + 0.9522 MSI MSI = 0.0095 + 0.9938 OLI	65,380,633	0.9462 (< 0.0001)	–0.0081	–3.56
Shortwave infrared λ (~2.21 μm)	OLI = 0.0004 + 0.9711 MSI MSI = 0.0065 + 0.9844 OLI	65,380,028	0.9560 (< 0.0001)	–0.0041	–2.95
NDVI	OLI = 0.0185 + 0.9566 MSI MSI = 0.0016 + 1.0016 OLI	65,371,886	0.9582 (< 0.0001)	–0.0024	–0.24

coverage, medium spatial resolution, near daily time series science and applications. Combined use of different sensor data can be undertaken in a number of different ways, including sensor data fusion into a single new data set, or by transforming the data from one sensor so that they are more similar to the other sensor's data. This paper focused on the latter approach. There are a number of pre-processing issues that need to be addressed before the well calibrated Landsat-8 and Sentinel-2 data (Markham et al., 2014; Mishra et al., 2016; Gascon et al., 2017) can be used together or treated as effectively being sensed from the same sensor. The Sentinel-2 MSI and Landsat-8 OLI data have quite different sensor spectral response functions and some bands that are not common, including the MSI red-edge bands (Drusch et al., 2012) that were not considered in this study as they are not acquired by the OLI (Irons et al., 2012). The Sentinel-2 MSI has 10 m and 20 m bands and there are six approximately spectrally equivalent Landsat-8 OLI 30 m bands. To handle this spatial resolution difference, the Sentinel-2 10 m and 20 m data could be resampled to Landsat-8 30 m resolution, or the Landsat-8 data could be downsampled to Sentinel-2 resolution (Li et al., 2017b). In this study, the MSI and OLI sensor data were registered precisely (Yan et al., 2018) and reprojected to 30 m in the same equal area projection. This was necessary because the MSI and OLI sensor data are defined in different tiling schemes with different map projections (UTM zones) and, at the time of writing, are not well registered for direct comparison without additional registration (Yan et al., 2016; Storey et al., 2016; Skakun et al., 2017; Gascon et al., 2017). Atmospheric correction of optical wavelength data is usually considered necessary due to the variable nature of atmospheric scattering and absorbing constituents. In particular aerosols are highly variable in space and time and are often difficult to characterize (Dubovik et al., 2002). In this study the same recent atmospheric characterization and radiative transfer based atmospheric correction approach, LaSRC (Land Surface Reflectance Code) that includes an image based spatially explicit aerosol retrieval (Vermote et al., 2016), was applied to the MSI and OLI TOA data. The MSI and the OLI surface reflectance data were corrected to surface NBAR using the same MODIS-based c -factor approach to reduce BRDF effects known to be present in their data (Roy et al., 2016a, 2017).

The above processing was applied to two summer and two winter months of contemporaneous Sentinel-2A MSI and Landsat-8 OLI observations sensed over 1200×1200 km of southern Africa. Only pairs of MSI and OLI pixel observations that were both not cloudy, shadow,

or cirrus contaminated, and that were acquired within one-day of each other, were considered to minimize the impact of surface and atmospheric changes. This enabled the meaningful comparison of approximately 65 million pairs of contemporaneous MSI and OLI observations. Statistical functions to transform between Sentinel-2A MSI and Landsat-8 OLI TOA reflectance, surface reflectance, and surface NBAR, were defined by ordinary least squares (OLS) linear regression. In addition, the NDVI derived from the results of the three processing levels was compared; the MSI NDVI was calculated using the narrow MSI band as it is spectrally more similar to the OLI NIR band. All of the OLS regressions had good fits ($r^2 > 0.87$ for TOA reflectance and NDVI comparisons, $r^2 > 0.89$ for surface reflectance and surface NDVI comparisons, $r^2 > 0.90$ for surface NBAR and surface NBAR NDVI comparisons) and were significant (p -values < 0.0001). Thus, the OLS transformation coefficients can be applied to broadly normalize the data (TOA reflectance, surface reflectance, surface NBAR, and derived NDVI) of one sensor to the other.

Simulated Sentinel-2A MSI and Landsat-8 OLI reflectance derived using the sensor spectral response functions (version 3.0 released December 19th 2017 for Sentinel-2A) and a large number of laboratory spectra were compared to provide insights into the sensor differences. The differences were small but reduced major axis (RMA) regression indicated that MSI simulated reflectance was generally greater than simulated OLI reflectance for all the bands except the broad MSI NIR band. The RMA regression of the MSI broad band NIR (785–900 nm) and the OLI NIR (851–879 nm) indicated that the MSI reflectance was generally smaller than the OLI reflectance and this was attributed to the very different spectral band passes. The simulated NDVI data RMA regressions indicated similar sensor data.

The 65 million pairs of Sentinel-2A MSI and Landsat-8 OLI TOA reflectance values considered in this study likely had differences due not only to sensor spectral response function differences, but also to atmospheric contamination, calibration, and sensing geometry (i.e., bi-directional reflectance) differences. The TOA RMA regression slopes were generally similar to those for the simulated data but with slopes further from unity because of these factors. Compared to the simulated data, the blue band RMA slope changed from below unity to above unity, and the broad band NIR and the NDVI RMA slopes increased further above unity. This is likely due to atmospheric contamination which is particularly severe at blue wavelengths (due to aerosol scattering) and in the MSI broad band NIR (due to water vapor absorption).

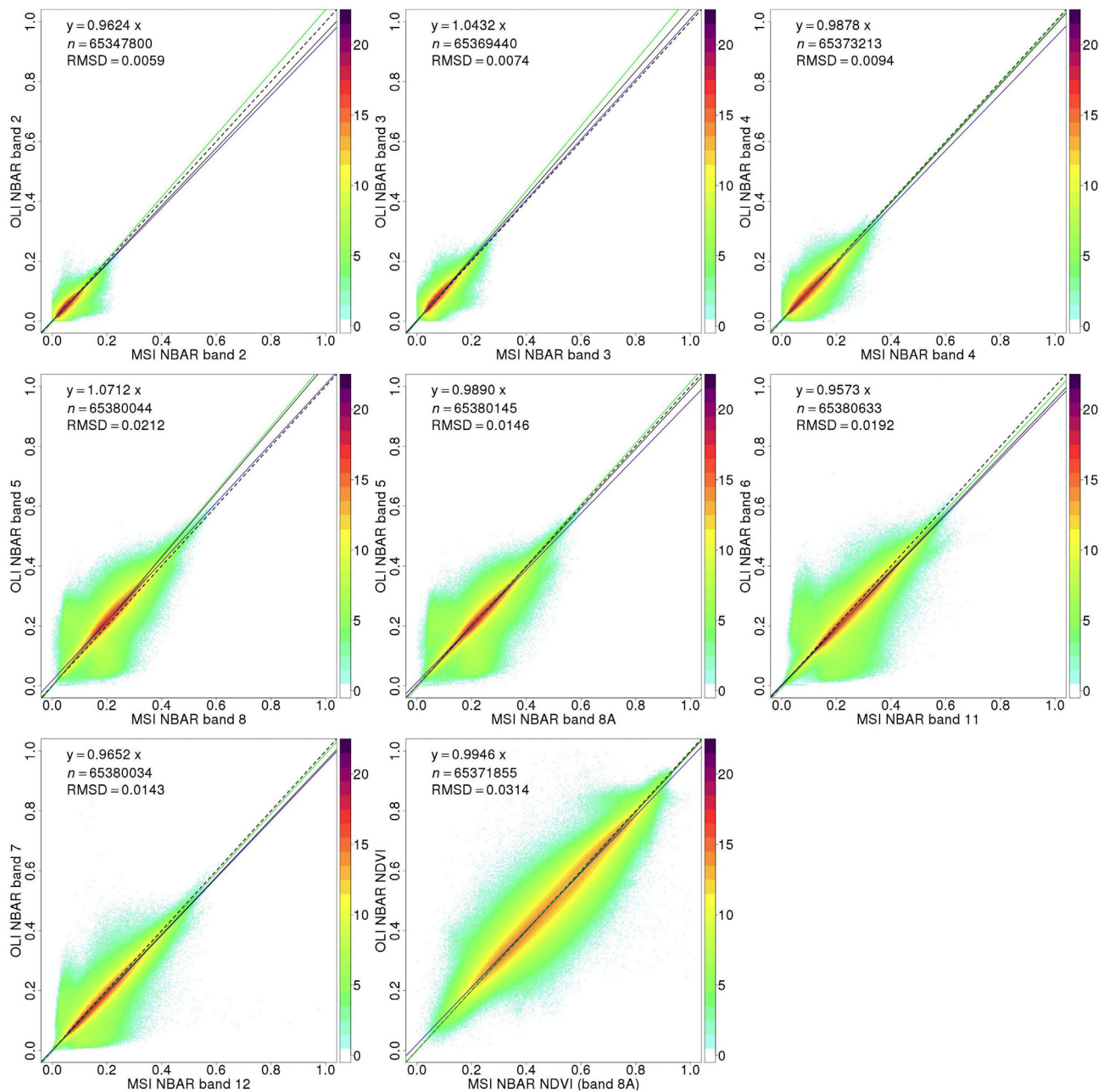


Fig. 6. As Fig. 4 but showing the atmospherically corrected data adjusted to a nadir view and the observed solar zenith, i.e., surface NBAR and surface NBAR NDVI.

Further, the MSI and OLI TOA reflectance mean relative differences were for all bands (except the broad band MSI NIR band comparison) comparable in magnitude to the better than 3% Landsat-8 OLI and Sentinel-2A MSI on orbit calibration performance (Markham et al., 2014; Gascon et al., 2017).

The LaSRC atmospheric correction to surface reflectance increased the range of the surface reflectance and NDVI. This increased range has been observed in other studies and is expected due to the spectral dependency of atmospheric effects on TOA reflectance with the spectral albedo of the surface (Tanre et al., 1981). The MSI surface reflectance was greater than the OLI surface reflectance for all the bands except the green, red, and broad band NIR bands. The MSI surface NDVI was generally greater than the OLI surface NDVI. We note that atmospheric correction is never perfect, particularly at shorter wavelengths where atmospheric impacts are usually greatest (Ju et al., 2012; Claverie et al., 2015). This was the case in this study - the surface reflectance mean relative differences between the sensors were greatest for the shortest

wavelength blue (4.64%) and green (4.80%) bands. Non-random atmospheric correction errors may become apparent when the surface reflectance from two observations of the same location is compared. A concern is that non-random atmospheric correction errors may occur differently in the MSI and OLI LaSRC corrected data. Indeed, careful inspection of the study data, indicates that there may be a LaSRC over-correction of the $\sim 1.62 \mu\text{m}$ SWIR bands, although this could also be related to sensor calibration issues. Further work to investigate this is recommended.

The *c*-factor MODIS-based BRDF correction algorithm was demonstrated independently for Landsat-8 OLI (Roy et al., 2016a) and Sentinel-2A data (Roy et al., 2017) and this study further confirms that the algorithm provides a bulk correction for viewing angle BRDF effects in these sensors. Correction of the MSI and OLI surface reflectance to surface NBAR reduced the scatter in the data with increased OLS regression r^2 values for all the reflective bands. Notably, likely due to the greater view zenith angle range in Sentinel-2A MSI data ($\pm 10.3^\circ$)

Table 4

Sentinel-2A MSI and Landsat-8 OLI surface NBAR and surface NBAR NDVI sensor transformation functions for the approximately equivalent spectral bands (Table 1) derived by ordinary least squares (OLS) regression of the data illustrated in Fig. 6. The number of pairs of sensor values considered (n), the regression coefficient of determination (r^2) and F-test p -value, and mean difference (Eq. (4)) and mean relative difference (Eq. (5)) between the OLI and MSI data are tabulated.

Between sensor OLS transformation functions and regression coefficients		n	OLS r^2 (p -value)	Mean OLI – MSI difference ($\bar{\Delta}$) (units: reflectance 0–1, or NDVI 0–1)	Mean relative OLI – MSI difference ($\bar{\Delta}^*$) (units: %)
Blue λ (~0.48 μm)	OLI = 0.0006 + 0.9420 MSI MSI = 0.0034 + 0.9584 OLI	65,347,800	0.9028 (< 0.0001)	–0.0018	–5.42
Green λ (~0.56 μm)	OLI = 0.0022 + 1.0078 MSI MSI = 0.0028 + 0.9162 OLI	65,369,440	0.9233 (< 0.0001)	0.0026	3.76
Red λ (~0.66 μm)	OLI = 0.0041 + 0.9435 MSI MSI = 0.0001 + 1.0058 OLI	65,373,213	0.9489 (< 0.0001)	–0.0006	–0.34
Near infrared λ (~0.85 μm) MSI Band 8	OLI = 0.0172 + 0.9898 MSI MSI = 0.0025 + 0.9207 OLI	65,380,044	0.9113 (< 0.0001)	0.0151	7.16
Near infrared λ (~0.85 μm) MSI Band 8A	OLI = 0.0111 + 0.9400 MSI MSI = 0.0069 + 0.9796 OLI	65,380,145	0.9208 (< 0.0001)	–0.0024	–1.03
Shortwave infrared λ (~1.61 μm)	OLI = 0.0032 + 0.9433 MSI MSI = 0.0073 + 1.0136 OLI	65,380,633	0.9562 (< 0.0001)	–0.0104	–4.54
Shortwave infrared λ (~2.21 μm)	OLI = 0.0007 + 0.9586 MSI MSI = 0.0051 + 1.0044 OLI	65,380,034	0.9628 (< 0.0001)	–0.0058	–4.02
NDVI	OLI = 0.0197 + 0.9555 MSI MSI = 0.0004 + 1.0027 OLI	65,371,855	0.9581 (< 0.0001)	–0.0017	–0.07

compared to Landsat-8 OLI data ($\pm 7.5^\circ$), the BRDF correction generally decreased the OLI against MSI OLS regression slopes and increased the MSI against OLI OLS regression slopes. Thus, as for the surface reflectance data, the MSI surface NBAR was generally greater than the OLI surface NBAR reflectance for all the bands except the green and broad band NIR bands. The BRDF correction did not have a significant impact on the NDVI results and the MSI surface NBAR NDVI was generally greater than the OLI surface NBAR NDVI.

The between sensor transformations derived from the OLS regressions are provided (Tables 2, 3 and 4) so that users may use them to improve the consistency between the Sentinel-2A MSI and Landsat-8 OLI data. Further work is required to examine whether they will also be applicable to the recently launched Sentinel-2B MSI data. Please note that the v3.5.5 LaSRC atmospheric correction software used Version 2.0 (released before December 19th 2017) Sentinel-2A spectral response functions (Version 3.0 is illustrated in Fig. 1) and the L1C Sentinel-2A TOA reflectance data were also processed by ESA using Version 2.0. Unfortunately, this version of the spectral response functions was found recently to have anomalies that affect primarily the MSI blue and broad NIR bands (MSI bands 1, 2 and 8) but with negligible impact on the L1C Sentinel-2A TOA reflectance (Clerc and MPC Team, 2018). Thus, although the Sentinel-2A TOA and surface reflectance considered in this study were retrieved with consistent spectral response functions, biases with respect to the Landsat-OLI equivalent wavelength bands may be present. In particular, biases in the reported statistical relationships between the MSI blue (band 2) and the OLI blue (band 2) surface reflectance, and between the MSI broad NIR (band 8) and the OLI NIR (band 5) surface reflectance, may be present. These biases are likely to be smaller than uncertainties imposed by aerosols in the blue band atmospheric correction and imposed by the significant spectral bandwidth difference between MSI band 8 (115 nm) and OLI band 5 (29 nm). They are also likely to be smaller than the MSI and OLI calibration errors. Further work in these respects is recommended using consistent Sentinel-2A spectral response function knowledge.

A large number of pairs of MSI and OLI screened pixel observations (> 65 million extracted from a 1,440,000 km² study area over a range of land cover types) were considered (Section 2.2) and so exhibited a considerable range of reflectance values (Figs. 4–6). The OLS transformations derived in this paper may be less appropriate however for geographic areas with different vegetation communities or soil types. For example, this study did not consider evergreen needleleaf and snow

and ice land covers. Mandanici and Bitelli (2016) reported Landsat-8 and Sentinel-2A between sensor transformations for five study areas, each about 1500 km² with different predominant land covers, and observed different transformations among the study areas. In addition, observations sensed under very high solar zenith conditions, that may affect the atmospheric correction and NBAR derivation (Roy et al., 2017), were not considered and the OLS transformations may be less appropriate for these sensing conditions. If different atmospheric correction and BRDF correction algorithms are used to process the Sentinel-2A MSI and Landsat-8 OLI data then the surface and surface NBAR transformations may also be less appropriate if the algorithms do not have similar performance to the ones used in this study.

Acknowledgements

This research was funded by the NASA Land Cover/Land Use Change Multi-Source Land Imaging Science Program Grant NNX15AK94G. The European Space Agency and Copernicus program management and staff, and the USGS Landsat program management and staff, are thanked for the free provision of the Sentinel-2A and Landsat-8 data respectively.

References

- Arvidson, T., Gasch, J., Goward, S.N., 2001. Landsat 7's long-term acquisition plan - an innovative approach to building a global imagery archive. *Remote Sens. Environ.* 78, 13–26.
- Baldrige, A.M., Hook, S.J., Grove, C.I., Rivera, G., 2009. The ASTER spectral library version 2.0. *Remote Sens. Environ.* 113, 711–715.
- Barsi, J.A., Lee, K., Kvaran, G., Markham, B.L., Pedelty, J.A., 2014. The spectral response of the Landsat-8 operational land imager. *Remote Sens.* 6, 10232–10251.
- Clark, R.L., Swayze, G.A., Wise, R., Livo, K.E., Hoefen, T., Kokaly, R.F., Sutley, S.J., 2007. USGS Digital Spectral Library splib06a. U.S. Geological Survey. <http://speclab.cr.usgs.gov/spectral.lib06>.
- Claverie, M., Vermote, E.F., Franch, B., Masek, J.G., 2015. Evaluation of the Landsat-5 TM and Landsat-7 ETM+ surface reflectance products. *Remote Sens. Environ.* 169, 390–403.
- Clerc, S., MPC Team, 2018. Sentinel-2 Data Quality Report, Accessed on April 10th 2018 Online. <https://sentinel.esa.int/documents/247904/685211/Sentinel-2-Data-Quality-Report> (Issue 25, ESA REF: S2-PDGS-MPC-DQR, Date 11 April 5th 2018, 37 pages).
- Drusch, M., Del Bello, U., Carlier, S., Colin, O., Fernandez, V., Gascon, F., Hoersch, B., Isola, C., Laberinti, P., Martimort, P., Meygret, A., Spoto, F., Sya, O., Marchese, F., Bargellini, P., 2012. Sentinel-2: ESA's optical high-resolution mission for GMES operational services. *Remote Sens. Environ.* 120, 25–36.
- Dubovik, O., Holben, B., Eck, T.F., Smirnov, A., Kaufman, Y.J., King, M.D., Tanré, D.,

- Slutsker, I., 2002. Variability of absorption and optical properties of key aerosol types observed in worldwide locations. *J. Atmos. Sci.* 59 (3), 590–608.
- ENVI, 2013. ENVI 5.1 Spectral Library Readme Files. Assessed in the Installation Directory of ENVI 5.1.
- ESA (European Space Agency), 2015. Sentinel-2 User Handbook, Issue 1, Revision 2, 24/07/2015. ESA Standard Document.
- Flood, N., 2017. Comparing sentinel-2A and Landsat 7 and 8 using surface reflectance over Australia. *Remote Sens.* 9 (7), 659.
- Foga, S., Scaramuzza, P.L., Guo, S., Zhu, Z., Dilley, R.D., Beckmann, T., Schmidt, G.L., Dwyer, J.L., Hughes, J.M., Laue, B., 2017. Cloud detection algorithm comparison and validation for operational Landsat data products. *Remote Sens. Environ.* 194, 379–390.
- Friedl, M.A., Sulla-Menashé, D., Tan, B., Schneider, A., Ramankutty, N., Sibley, A., Huang, X., 2010. MODIS Collection 5 global land cover: algorithm refinements and characterization of new datasets. *Remote Sens. Environ.* 114, 168–182.
- Gao, F., Jin, Y., Schaaf, C.B., Strahler, A.H., 2002. Bidirectional NDVI and atmospherically resistant BRDF inversion for vegetation canopy. *IEEE Trans. Geosci. Remote Sens.* 40 (6), 1269–1278.
- Gao, F., He, T., Masek, J.G., Shuai, Y., Schaaf, C.B., Wang, Z., 2014. Angular effects and correction for medium resolution sensors to support crop monitoring. *IEEE J. Sel. Topics Appl. Earth Observ. Remote Sens.* 7 (11), 4480–4489.
- Gascon, F., Bouzinac, C., Thépaut, O., Jung, M., Francesconi, B., Louis, J., Lonjou, V., Lafrance, B., Massera, S., Gaudel-Vacaresse, A., Languille, F., Alhammoud, B., Viallefond, F., Pflug, B., Bieniarz, J., Clerc, S., Pessiot, L., Trémas, T., Cadau, E., De Bonis, R., Isola, C., Martimort, P., Fernandez, V., 2017. Copernicus sentinel-2 calibration and products validation status. *Remote Sens.* 9, 584.
- Gorroño, J., Banks, A.C., Fox, N.P., Underwood, C., 2017. Radiometric inter-sensor cross-calibration uncertainty using a traceable high accuracy reference hyperspectral imager. *ISPRS J. Photogramm. Remote Sens.* 130, 393–417.
- Hagolle, O., Huc, M., Pascual, D.V., Dedieu, G., 2010. A multi-temporal method for cloud detection, applied to FORMOSAT-2, VENUS, LANDSAT and SENTINEL-2 images. *Remote Sens. Environ.* 114 (8), 1747–1755.
- Hagolle, O., Huc, M., Villa Pascual, D., Dedieu, G., 2015. A multi-temporal and multi-spectral method to estimate aerosol optical thickness over land, for the atmospheric correction of formosat-2, Landsat, venus and Sentinel-2 images. *Remote Sens.* 7 (3), 2668–2691.
- Houborg, R., McCabe, M.F., 2017. Impacts of dust aerosol and adjacency effects on the accuracy of Landsat 8 and RapidEye surface reflectances. *Remote Sens. Environ.* 194, 127–145.
- Irish, R.R., Barker, J.L., Goward, S.N., Arvidson, T., 2006. Characterization of the Landsat-7 ETM+ automated cloud-cover assessment (ACCA) algorithm. *Photogramm. Eng. Remote Sens.* 72, 1179–1188.
- Irons, J.R., Dwyer, J.L., Barsi, J.A., 2012. The next Landsat satellite: the Landsat data continuity mission. *Remote Sens. Environ.* 122, 11–21.
- Ju, J., Roy, D.P., Vermote, E., Masek, J., Kovalsky, V., 2012. Continental-scale validation of MODIS-based and LEDAPS Landsat ETM+ atmospheric correction methods. *Remote Sens. Environ.* 122, 175–184.
- Kaufman, Y.J., Gao, B.C., 1992. Remote sensing of water vapor in the near IR from EOS/MODIS. *IEEE Trans. Geosci. Remote Sens.* 30 (5), 871–884.
- Li, J., Roy, D.P., 2017. A global analysis of sentinel-2A, sentinel-2B and Landsat-8 data revisit intervals and implications for terrestrial monitoring. *Remote Sens.* 9 (9), 902.
- Li, S., Ganguly, S., Dungan, J.L., Wang, W., Nemani, R.R., 2017a. Sentinel-2 MSI radiometric characterization and cross-calibration with Landsat-8 OLI. *Adv. Remote Sens.* 6 (02), 147.
- Li, Z., Zhang, H.K., Roy, D.P., Yan, L., Huang, H., Li, J., 2017b. Landsat 15-m panchromatic-assisted downscaling (LPAD) of the 30-m reflective wavelength bands to Sentinel-2 20-m resolution. *Remote Sens.* 9 (7), 755.
- Liang, S., Fang, H., Chen, M., 2001. Atmospheric correction of Landsat ETM+ land surface imagery. I. Methods. *IEEE Trans. Geosci. Remote Sens.* 39 (11), 2490–2498.
- Loveland, T.R., Irons, J.R., 2016. Landsat 8: the plans, the reality, and the legacy. *Remote Sens. Environ.* 185, 1–6.
- Mandanici, E., Bitelli, G., 2016. Preliminary comparison of Sentinel-2 and Landsat 8 imagery for a combined use. *Remote Sens.* 8 (12), 1014.
- Markham, B., Barsi, J., Kvaran, G., Ong, L., Kaita, E., Biggar, S., Czaplá-Myers, J., Mishra, N., Helder, D., 2014. Landsat-8 operational land imager radiometric calibration and stability. *Remote Sens.* 6 (12), 12275–12308.
- Marshak, A., Wen, G., Coakley, J.A., Remer, L.A., Loeb, N.G., Cahalan, R.F., 2008. A simple model for the cloud adjacency effect and the apparent bluing of aerosols near clouds. *J. Geophys. Res.-Atmos.* 113 (D14).
- Masek, J.G., Vermote, E.F., Saleous, N.E., Wolfe, R., Hall, F.G., Huemmrich, K.F., Gao, F., Kutler, J., Lim, T.K., 2006. A Landsat surface reflectance dataset for North America, 1990–2000. *IEEE Geosci. Remote Sens. Lett.* 3 (1), 68–72.
- Mishra, N., Helder, D., Barsi, J., Markham, B., 2016. Continuous calibration improvement in solar reflective bands: Landsat 5 through Landsat 8. *Remote Sens. Environ.* 185, 7–15.
- Miura, T., Huete, A.R., Yoshioka, H., 2000. Evaluation of sensor calibration uncertainties on vegetation indices for MODIS. *IEEE Trans. Geosci. Remote Sens.* 38, 1399–1409.
- Müller-Wilm, U., 2016. Sen2Cor Configuration and User Manual, Ref. S2-PDGS-MPC-L2A-SUM-V2.3, Telespazio VEGA Deutschland GmbH: Darmstadt, Germany.
- Ouaidrari, H., Vermote, E.F., 1999. Operational atmospheric correction of Landsat TM data. *Remote Sens. Environ.* 70, 4–15.
- Richter, R., Louis, J., Müller-Wilm, U., 2012. Algorithm Sentinel-2 MSI – Level 2A Products Algorithm Theoretical Basis Document.S2PADATBD-0001, Issue 2.0.
- Roy, D.P., Wulder, M., Loveland, T., Woodcock, C., Allen, R., Anderson, M., Helder, D., Irons, J., Johnson, D., Kennedy, R., Scambos, T., Schaaf, C.B., Schott, J.R., Sheng, Y., Vermote, E.F., Belward, A.S., Bindschadler, R., Cohen, W.B., Gao, F., Hipple, J.D., Hostert, P., Huntington, J., Justice, C.O., Kilic, A., Kovalsky, V., Lee, Z.P., Lybumbur, L., Masek, J.G., McCorkel, J., Shuai, Y., Trezza, R., Vogelmann, J., Wynne, R.H., Zhu, Z., 2014a. Landsat-8: science and product vision for terrestrial global change research. *Remote Sens. Environ.* 145, 154–172.
- Roy, D.P., Qin, Y., Kovalsky, V., Vermote, E.F., Ju, J., Egorov, A., Hansen, M.C., Kommareddy, I., Yan, L., 2014b. Conterminous United States demonstration and characterization of MODIS-based Landsat ETM+ atmospheric correction. *Remote Sens. Environ.* 140, 433–449.
- Roy, D., Zhang, H., Ju, J., Gomez-Dans, J., Lewis, P., Schaaf, C., Sun, Q., Li, J., Huang, H., Kovalsky, V., 2016a. A general method to normalize Landsat reflectance data to nadir BRDF adjusted reflectance. *Remote Sens. Environ.* 176, 255–271.
- Roy, D.P., Kovalsky, V., Zhang, H.K., Vermote, E.F., Yan, L., Kumar, S.S., Egorov, A., 2016b. Characterization of Landsat-7 to Landsat-8 reflective wavelength and normalized difference vegetation index continuity. *Remote Sens. Environ.* 185, 57–70.
- Roy, D.P., Li, J., Zhang, H.K., Yan, L., 2016c. Best practices for the reprojection and resampling of Sentinel-2 Multi Spectral Instrument Level 1C data. *IEEE Geosci. Remote Sens. Lett.* 7 (11), 1023–1032.
- Roy, D.P., Li, J., Zhang, H.K., Yan, L., Huang, H., Li, Z., 2017. Examination of Sentinel-2A multi-spectral instrument (MSI) reflectance anisotropy and the suitability of a general method to normalize MSI reflectance to nadir BRDF adjusted reflectance. *Remote Sens. Environ.* 199, 25–38.
- Skakun, S., Roger, J.C., Vermote, E.F., Masek, J.G., Justice, C.O., 2017. Automatic sub-pixel co-registration of Landsat-8 operational land imager and sentinel-2A multi-spectral instrument images using phase correlation and machine learning based mapping. *Int. J. Digital Earth* 1–17.
- Smith, R.J., 2009. Use and misuse of the reduced major axis for line-fitting. *Am. J. Phys. Anthropol.* 140, 476–486.
- Steven, M.D., Malthus, T.J., Baret, F., Xu, H., Chopping, M.J., 2003. Intercalibration of vegetation indices from different sensor systems. *Remote Sens. Environ.* 88, 412–422.
- Storey, J., Roy, D.P., Masek, J., Gascon, F., Dwyer, J., Choate, M., 2016. A note on the temporary mis-registration of Landsat-8 Operational Land Imager (OLI) and Sentinel-2 Multi Spectral Instrument (MSI) imagery. *Remote Sens. Environ.* 186, 121–122.
- Tackett, J.L., Di Girolamo, L., 2009. Enhanced aerosol backscatter adjacent to tropical trade wind clouds revealed by satellite-based lidar. *Geophys. Res. Lett.* 36 (14).
- Tanre, D., Herman, M., Deschamps, P., 1981. Influence of the background contribution upon space measurements of ground reflectance. *Appl. Opt.* 20, 3676–3684.
- Ustin, S.L., Roberts, D.A., Pinzon, J., Jacquemoud, S., Gardner, M., Scheer, G., Castaneda, C.M., Palacios-Orueta, A., 1998. Estimating canopy water content of chaparral shrubs using optical methods. *Remote Sens. Environ.* 65, 280–291.
- Vermote, E.F., Tanré, D., Deuze, J.L., Herman, M., Morcette, J.J., 1997. Second simulation of the satellite signal in the solar spectrum, 6S: an overview. *IEEE Trans. Geosci. Remote Sens.* 35 (3), 675–686.
- Vermote, E.F., Justice, C., Claverie, M., Franch, B., 2016. Preliminary analysis of the performance of the Landsat 8/OLI land surface reflectance product. *Remote Sens. Environ.* 185, 46–56.
- Wolfe, R.E., Roy, D.P., Vermote, E., 1998. MODIS land data storage, gridding, and compositing methodology: level 2 grid. *IEEE Trans. Geosci. Remote Sens.* 36, 1324–1338.
- Wulder, M.A., Hilker, T., White, J.C., Coops, N.C., Masek, J.G., Pflugmacher, D., Crevier, Y., 2015. Virtual constellations for global terrestrial monitoring. *Remote Sens. Environ.* 170, 62–76.
- Yan, L., Roy, D.P., Zhang, H.K., Li, J., Huang, H., 2016. An automated approach for sub-pixel registration of Landsat-8 Operational Land Imager (OLI) and Sentinel-2 Multi Spectral Instrument (MSI) imagery. *Remote Sens.* 8 (6), 520.
- Yan, L., Roy, D.P., Li, Z., Zhang, H.K., Huang, H., 2018. Sentinel-2A multi-temporal misregistration characterization and an orbit-based sub-pixel registration methodology. *Remote Sens. Environ.* <http://dx.doi.org/10.1016/j.rse.2018.04.021>.
- Zhang, H.K., Roy, D.P., 2016a. Computationally inexpensive Landsat 8 operational land imager (OLI) pansharpening. *Remote Sens.* 8 (3), 180.
- Zhang, H.K., Roy, D.P., 2016b. Landsat-5 Thematic Mapper reflectance and NDVI 27-year time series inconsistencies due to satellite orbit change. *Remote Sens. Environ.* 186, 217–233.